Assessing the Fracture and Fatigue Resistance of Nanostructured Thin Films

L. Zauner[1]*, R.Hahn[1], E. Aschauer[1], T. Wojcik[1,2], A. Davydok[3], O. Hunold[4], P. Polcik[5], and H. Riedl[1,2]

[1] Christian Doppler Laboratory for Surface Engineering of high-performance Components, TU Wien, Austria
[2] Institute of Materials Science and Technology, TU Wien, Austria
[3] Helmholtz-Zentrum Hereon, Institut für Werkstoffphysik, Germany
[4] Oerlikon Balzers, Oerlikon Surface Solutions AG, Liechtenstein
[5] Plansee Composite Materials GmbH, Germany

*L.Z. Corresponding Author, Author 1
Christian Doppler Laboratory for Surface Engineering of high-performance Components, TU Wien
Getreidemarkt 9
1060 Wien, Austria
lukas.zauner@tuwien.ac.at
+4315880130820
ORCID-ID: 0000-0002-8373-6552

R.H. Author 2
rainer.hahn@tuwien.ac.at

E.A. Author 3
e.aschauer@gmx.net

T.W. Author 4
tomasz.wojcik@tuwien.ac.at

A.D. Author 5
anton.davydok@hereon.de

O.H. Author 6
Oliver.Hunold@oerlikon.com

P.P. Author 7
Peter.Polcik@plansee.com

H.R. Author 8
helmut.riedl@tuwien.ac.at

1

Abstract

Fatigue failure caused by sustained loading of ductile materials manifests in irreversible motion of dislocations, followed by crack initiation and growth. This contrasts with the failure mechanisms associated with brittle ceramics, such as nanostructured physical vapor deposited thin films, where inhibited dislocation mobility typically leads to interface-controlled damage. Hence, understanding the fatigue response of thin films from a fundamental viewpoint – including altered atomic bonds, crystal structures, and available deformation mechanisms – holds the key to improved durability of coated engineering components. Here, a novel approach utilizing quasi-static and cyclic bending of pre-notched, unstrained microcantilever beams coupled with in-situ synchrotron X-ray diffraction is presented to study the fracture toughness and fatigue properties of thin films under various loading conditions. Investigating a model system of sputter deposited Cr and Cr-based ceramic compounds (CrN, CrB_2, and Cr_2O_3) demonstrates that the fatigue resistance of such thin films is limited by the inherent fracture toughness, irrespective of the prevalent bonding character or crystal structure. Moreover, as revealed by complementary micro-pillar compression tests, the fracture toughness is in clear connection with the elasto-plastic deformation behavior, thus elucidating the wide range of values from 1.6±0.2 up to 4.3±0.3 MPa√m for $Cr_{1.79}O_3$ and $Cr_{1.03}B_2$, respectively. In fact, cantilever cycling close to the critical stress intensity is sustained up to 10^7 load cycles on all materials, without inducing noticeable material damage, structural or stress-state changes. Our findings contribute key-insights into the underlying mechanisms dictating the damage tolerance of PVD coated components by relating fatigue strength limits to fundamental material properties.

2

1. Introduction

Creating a fundamental understanding of the fracture and fatigue resistance of state-of-the-art materials is invariably associated with predicting the accessible lifespan for engineering components in aerospace, electronics, or energy applications [1]. The term "fatigue" comprises the cumulative material damage induced by cyclic loading, frequently leading to fracture and failure of structural components. In metals, where plasticity takes the dominating role in controlling cyclic deformation, fatigue damage accumulates upon irreversible plastic flow, initiated by irreversible dislocation motion. The latter mechanism cumulates in the formation of cracks at preferential sites such as persistent slip bands and related surface irregularities (*i.e.*, intrusions or extrusions), high-angle grain boundaries, or twin-boundaries [2–5]. Conversely, on the opposite end of the ductility spectrum, highly brittle ceramic materials are characterized by strong ionic and/or covalent bonds with limited dislocation mobility. In turn, the resistance to fracture and fatigue failure in these brittle solids is inherently determined by the atomic bond strength and activation of pre-existing flaws (*i.e.*, grain boundaries, voids, inclusions, etc.) under loading [2,6,7]. Yet, regardless of the apparent bonding character, the material response under repeating loads is closely linked to the microstructure at hand.

Decreasing the overall microstructural domain size, as is the case for physical vapor deposited micro- or nanostructured thin films, it is obvious that the governing deformation mechanisms are affected by the increased fraction of interfaces, grain boundaries, and free surfaces. These features introduce additional constraints on the availability of dislocation sources, their activity, and mutual interaction so that macroscopic dislocation features are reduced and interface-mediated damage, similar to brittle materials, becomes prevalent [3,8–10].

While general, bulk-scale fracture toughness and fatigue experiments provide means of identifying the crack resistance and lifespan of a material, assessing the failure-responsible atomistic or structural origin is difficult to accomplish. Thus, shrinking the examined material volume to characteristic thin

3

film dimensions allows to fundamentally probe the influence of such features and unravel the origins of material failure [11–14].

Using micro sized cantilever beams and pillars, the intrinsic fracture toughness and failure strength of thin films – especially that of hard protective coatings – has been investigated extensively [15–22]. In contrast, reports on fatigue testing of coating materials are disproportionly less, with a strong focus towards metallic materials (*e.g.*, copper, nickel-base alloys, etc.) [23–27] or macroscale testing of the entire coating-substrate arrangement [28–34].

Employing TiN coated Ti-6Al-4V tension-tension fatigue specimen, Bai *et al.* [35] recently identified a stress-sensitive crack initiation mechanism. While below a critical stress amplitude dislocation pile-up and slip-steps in the substrate induced crack formation close to the coating interface, increasing the applied stress resulted in accelerated, coating-fracture-induced cleavage cracking of the substrate (see also Ref. [36]). Based on these mechanisms, enhancing the coating toughness or introducing a ductile interlayer is suggested to alleviate the adverse effect of the coating on the substrate fatigue properties. In addition, Sivagnanam Chandra *et al.* [37,38] discussed the influence of varying both the thickness and compressive stress state of Ti-Al-N coated Ti-alloys by correlating the observed fatigue failure with the imposed stress profile. There, critical aspects of the residual stress state across the coating and interface region were highlighted with respect to preferred crack nucleation sites.

Shifting the viewpoint to microscale fatigue testing, Kiener *et al.* [39] first performed fully-reversed *in situ* bending experiments on free standing single-crystalline copper micro cantilevers, thereby excluding any interference of substrates or microstructures with the resulting material behavior. The combined theoretical and experimental approach provided insights into the deformation mechanisms during fatigue loading at the micro-scale, up to a total number of $n = 100$ load cycles. Using an analogous approach for low cycle bending tests, a study by Kirchlechner *et al.* [3] coupled fatigue experiments of single-crystal copper beams with *in situ* synchrotron micro Laue diffraction to reveal the interplay of dislocation motion and slip planes under reversible load. Moreover, in works by

4

Wimmer *et al.* [40] and Lavenstein *et al.* [41], vastly increased numbers of load cycles were accessed for cantilever bending experiments on poly-crystalline copper ($n \sim 1.5 \times 10^5$) and a single-crystalline Ni-base superalloy ($n \sim 10^7$), respectively, providing insights into small-scale fatigue failure within the high cycle fatigue regime. Especially the approach of the latter study is unique in its utilization of a permanent bond between the actuator tip and cantilever free-end, which allows to maintain zero mean stress while avoiding load gaps during strain reversal. In addition, similar to a work by Schwaiger and Kraft [10], a stiffness based technique was employed to probe cyclic damage accumulation and discuss the fatigue crack evolution [42].

Despite the extent of studies carried out, only little is known about the micro-scale material response of cyclically loaded ceramic thin film materials. Especially the aspect of varying material classes, which includes altered interatomic bond characters, crystal structures, and hence available deformation mechanisms, lacks an in-depth understanding. In this study, various free-standing micro-geometries fabricated from Cr-based thin film materials (*i.e.*, body-centered cubic Cr, face-centered cubic CrN, hexagonal CrB_2, and rhombohedral Cr_2O_3) are utilized to unravel the fracture and fatigue properties of nanostructured thin films. Both, micro-cantilever bending and -pillar compression tests are conducted to discuss the apparent fracture resistance and elasto-plastic deformation behavior in relation to the structural properties. An approach based on synchrotron X-ray nanodiffraction coupled fatigue experiments reveals the in-plane stress distribution of statically and dynamically loaded microcantilevers. Moreover, the methodology provides a direct comparison between the observed high cycle fatigue properties and the individual single cycle strength, *i.e.*, the fracture toughness.

5

2. Experimental

2.1. Coating deposition

Cr-based thin films were deposited onto (100)-oriented silicon substrates by unbalanced DC magnetron sputtering (DCMS) using a modified Leybold Z400 deposition system. The metallic Cr as well as the CrN and Cr_2O_3 compound thin films were deposited from a powder-metallurgically prepared Cr target (99.95 % metallic purity, Plansee Composite Materials GmbH) operated in pure Ar-, mixed Ar/N_2-, or mixed Ar/O_2-atmosphere, respectively. The CrB_2 thin film was synthesized from a powder-metallurgically prepared CrB_2 target (99.3 % purity) in pure Ar-atmosphere. For all thin films, a constant target-to-substrate distance of 40 mm was maintained. Prior to each deposition, all substrates were ultrasonically pre-cleaned using acetone and ethanol consecutively. After reaching a base pressure of $p \leq 0.2$ mPa, the substrate was heated to the desired temperature T_{dep}, followed by an Ar-ion etching step with an applied substrate bias potential of U_S = -150 V (pulsed DC, 150kHz, 2496 ns pulse duration) at a total Ar gas pressure of p = 1.3 Pa. The subsequent depositions were carried out using parameters sets (*i.e.*, average cathode power density P_C, total deposition pressure p_{dep}, process gas composition, substrate bias potential U_S, etc.) determined during preliminary studies. Moreover, the deposition temperature (T_{dep}) was adjusted to maintain a uniform value of ~0.35 for the homologous temperature (T_H) of all Cr-based compounds, while that for metallic Cr was reduced to T_H ~0.22 to prevent extensive grain coarsening observed for higher T_H values. The deposition time was individually adjusted to yield a uniform thickness of h = 3 μm for all coatings. A summary of all deposition parameters and the resulting chemical composition including the content of undesired residuals *Res* (*i.e.*, argon and oxygen) are included in Table 1.

6

Table 1: Detailed overview of the deposition conditions and chemical composition of the synthesized coatings.

Coating	3" Target (purity, %)	P_C (Wcm^{-2})	T_{dep} (°C)	T_H (-)	p_{dep} (Pa)	Ar (sccm)	N$_2$ (sccm)	O$_2$ (sccm)	U_S (V)	Res (at.%)	H (GPa)	E (GPa)
Cr	Cr (99.95 %)	4.0	200	0.22 [43]	0.37	30	-	-	-75	≤ 0.8	9.4±0.3	308±7
Cr$_{0.94}$N	Cr (99.95 %)	4.6	400	0.34 [44]	0.37	16	16	-	-60	≤ 0.4	26.6±1.3	311±17
Cr$_{1.03}$B$_2$	CrB$_2$ (99.3 %)	5.5	600	0.35 [45]	0.37	30	-	-	-50	≤ 0.4	24.4±1.6	312±8
Cr$_{1.79}$O$_3$	Cr (99.95 %)	4.9	600	0.34 [46]	0.37	26	-	6.5	-50	≤ 0.6	31.8±1.8	306±8

2.2. Coating characterization

Investigations on the coating structure were conducted using X-ray diffraction (XRD) on a PANalytical XPert Pro MPD system equipped with a Cu-Kα radiation source (λ = 1.5418 Å) and operated in θ-θ geometry. The chemical composition of all Cr-based thin films was determined in top-view configuration by energy dispersive X-ray spectroscopy (EDS) utilizing an FEI Philips XL30 SEM equipped with an EDAX EDS detector (15 kV acceleration voltage). Furthermore, scanning electron microscopy (SEM) in an FEI Quanta 200 FEGSEM system (operated at 10 kV) was used to characterize the film growth morphology based on fracture cross-sections of single-side coated silicon substrates. Complementary detailed information on the growth characteristics and grain size distribution was obtained via transmission electron microscopy (TEM) on an FEI TECNAI F20 system (200 kV acceleration voltage) utilizing samples prepared in top-view orientation. Both, the hardness (*H*) and Young's modulus (*E*) were determined by an ultra-micro indentation system (UMIS) equipped with a Berkovich diamond tip. For each thin film, at least 30 load-displacement curves were analyzed according to Oliver and Pharr [47] in a load range of 6 to 45 mN.

Micromechanical bending experiments were performed on cantilever geometries to characterize the critical fracture force (*F_C*) and fracture toughness (*K_IC*) of all thin films investigated. Therefore, the silicon substrate of a mirror polished fracture cross-section was initially dissolved in aqueous KOH (40 wt.% concentration at a temperature of 70 °C) to yield a section of free-standing thin film material.

Focused ion beam milling (FIB) using Ga$^+$-ions on an FEI Quanta 200 3D DBFIB system was subsequently employed to produce microcantilever geometries in accordance with the guidelines given in Ref. [48]. A beam current of 1 nA was used for initial milling sequences, subsequently reduced to 0.5 nA to minimize ion induced material damage. The cantilevers were produced to a final geometry of length (*l*) $\times$ width (*b*) $\times$ height (*h*) = 22 $\times$ 3 $\times$ 3 µm^3, respectively. An initial notch was fabricated at a beam current of 50 pA. During testing, the cantilevers were loaded with an *in situ* FemtoTools FT-NMT04 nanoindentation system equipped with a diamond wedge tip (contact length of 10 µm) in an FEI Quanta 200 FEGSEM. The experiments were performed in displacement-controlled mode with a deflection rate of 5 nms^{-1}, so that the maximum force at failure (*i.e.*, F_C) could be determined. All load-displacement curves were further analyzed to assure pure linear-elastic material behavior. The fracture toughness was then evaluated according to Matoy *et al.* [15]:

$$K_{IC} = \frac{F_C l}{bh^{\frac{3}{2}}} \times f(\frac{a}{h}) \tag{1}$$

with

$$f\left(\frac{a}{h}\right) = 1.46 + 24.36\left(\frac{a}{h}\right) - 47.21\left(\frac{a}{h}\right)^2 + 75.18\left(\frac{a}{h}\right)^3 \quad , \tag{2}$$

where *a* is the depth of the initial notch. A total of five bending experiments were performed for each material system.

Furthermore, using a micropillar geometry, all coating materials were investigated in their plastic deformation response under uniaxial compression. The micropillars were analogously prepared by FIB milling of the as-deposited coatings at a height to diameter aspect ratio of *h*:*d* ~ 3:2 (*h* equals the coating thickness) and a taper angle below 2°. Stepwise decreased ion-currents from 15 nA to 50 pA were employed for coarse and fine milling, respectively. The pillars were compressed in displacement-controlled mode at 5 nms^{-1} using a diamond flat punch tip (contact diameter of 5 µm) mounted to the above mentioned *in situ* nanoindentation system. The recorded load - displacement curves were used

8

to calculate the engineering stress following an approach by Wheeler and Michler [49], where the top diameter of the pillar is taken as the reference contact area. The engineering strain was obtained from the displacement data using the coating thickness as the initial pillar height reference. Moreover, the displacement data was corrected by accounting for the base compliance following Sneddon's correction[50] given by

$$\Delta L_{Sneddon} = \frac{1 - \nu_{Sub}^2 F}{E_{Sub} \quad d} \quad , \quad (3)$$

where ν_{Sub} and E_{Sub} are the Poisson's ratio and Young's modulus of the substrate, respectively, and F is the applied force.

Additional investigations on the fatigue resistance of all Cr-based coatings under oscillating, unidirectional load were performed through cyclic cantilever bending experiments (*i.e.*, fatigue tests), employing the same cantilever specimen and nanoindentation system. The test setup was targeted towards cyclically loading the cantilever close to the instantaneous fracture threshold – within the boundaries given by geometrical deviations between the samples and thus differences in the actual fracture limit – to promote the accumulation of fatigue damage in the material and eventually cause failure of the micro specimen. Therefore, the oscillating force $F(t)$ was based on the previously recorded, material specific critical stress intensity, consisting of a mean force F_M = 0.75 × F_C overlaid with a sinusoidal amplitude force F_A = 0.15 × F_C. This resulted in the applied stress intensity oscillating between 60 and 90 % of K_{IC}, where a margin of 10 % was maintained to accommodate for any geometrical inconsistencies between the cantilevers. The fatigue tests were conducted in force-controlled mode, meaning that F_M and F_A are maintained throughout the test duration, irrespective of any cantilever deterioration (*i.e.*, crack growth). Furthermore, all experiments were performed at a loading frequency of f = 500 Hz for a duration of t = 334 min, which equates to a total number of n = 10[7] load cycles. In addition to the load - displacement data, also the dynamic cantilever stiffness S was recorded, which is defined as the real part of the ratio between the applied force- and displacement-amplitude (w_A) and takes the form:

9

$$S = \frac{F_A(t)}{w_A(t)}\cos(\varphi) \quad , \tag{4}$$

where φ denotes the phase angle between the load and displacement response. Within the framework of this work, changes to the parameter "stiffness" are used as the main indicator for cyclic degradation of the cantilever specimen.

2.3. Coupled synchrotron X-ray nanodiffraction and fatigue experiments

Initially, a double-side polished, cross-sectional substrate-coating lamella with a thickness of ~35 μm in beam direction was prepared by mechanical polishing of a $Cr_{0.94}N$ coated Si substrate. The lamella was subsequently secured to a sample holder, which allows for a precise horizontal alignment, guaranteeing a 90° contact angle of the coating surface to the nanoindenter tip, while avoiding any interference with diffracted beam paths during *in situ* cross-sectional X-ray nanodiffraction experiments (see Figure 1a). Using the above-mentioned FIB workstation, larger microcantilever specimens with a dimension of $l \times b \times h = 25 \times 25 \times 3$ μm³ were ion-milled into the sample lamella. Therefore, a gradually reduced Ga^+-ion current of 20, 5, and 1 nA was employed to remove the silicon substrate material underneath the coating on a length of 30 μm, producing a clamped cantilever of the coating material. The final geometry of the cantilever (*i.e.*, releasing one of the clamped ends, milling the contour to final shape) was fabricated at an ion-current of 1 nA. Analogous to the smaller cantilever specimens, an initial pre-crack was introduced in the form of a through-thickness notch at a beam current of 0.1 nA. Prior to the fatigue experiments, conventional bending tests were performed on three of these cantilevers to determine a new reference value for F_C and $K_{IC}*$. Here it is important to mention that the fracture toughness evaluation for $K_{IC}*$ is conducted outside the geometrical boundaries given in Ref. [15], with the sole purpose of obtaining the apparent fracture limit of the material in the given geometry.

10

The coupled synchrotron X-ray nanodiffraction and fatigue experiments were performed at the nanofocus endstation of beamline P03 at PETRA III located within the synchrotron facility "Deutsches Elektronen-Synchrotron" DESY (Hamburg, GERMANY). The monochromatic X-ray source was operated at a wavelength of λ = 0.82656 Å (beam energy of ~15 keV) and focused to a probe cross-section of ~250 nm. The above mentioned nanoindentation system was fixtured inside the measurement endstation such that the cantilever samples were placed in transmission geometry with the X-ray beam in line to the pre-notch [51]. Furthermore, the X-ray beam was centered at the pre-notch position, while the diamond wedge tip of the indenter system was located ~23 µm from this position at the opposite end and centered along the cantilever width (see Figures 1a and b). Positioning of the entire nanoindenter-sample arrangement was conducted using a hexapod (tilt alignment) and linear nanopositioning stages (x-y- as well as z-alignment). The 2D diffraction signals were recorded on an Eiger X M9 photon-counting detector, with an acquisition time of 10 s per frame. The exact detector arrangement with respect to the sample position was calibrated using a standardized LaB_6 reference powder, resulting in a fixed sample-detector distance of 319.2 mm. This allowed for the recording of diffraction patterns with Bragg angles of up to ~27°.

Area scans covering a 20 $\times$ 20 mesh-grid in steps of 300 nm along the y- and z-axis were performed prior to the fatigue experiments to characterize the cross-sectional area of the cantilever around the pre-notch position (see Figure 1c). Thereby, three different static loading scenarios were investigated, with the cantilever incrementally loaded from (*i*) no force applied, to (*ii*) ~35 % of K_{IC}* (not shown here), and to (*iii*) ~70 % of K_{IC}*. Subsequently, fatigue tests were conducted in alignment with the above-mentioned procedure and parameters, with the applied forces adjusted to F_M = 0.65 $\times$ F_C and F_A = 0.15 $\times$ F_C, respectively, resulting in the overall stress intensity oscillating between 50 and 80 % of K_{IC}*. During these experiments, three distinct positions along the cantilever height, spaced 1 µm apart (top, middle, bottom; see Figure 1d), were repeatedly scanned for the duration of the loading procedure. This allowed for a detailed analysis of the phase and stress evolution within the cantilever material up to a total number of n = 5 $\times$ 10^6 load cycles.
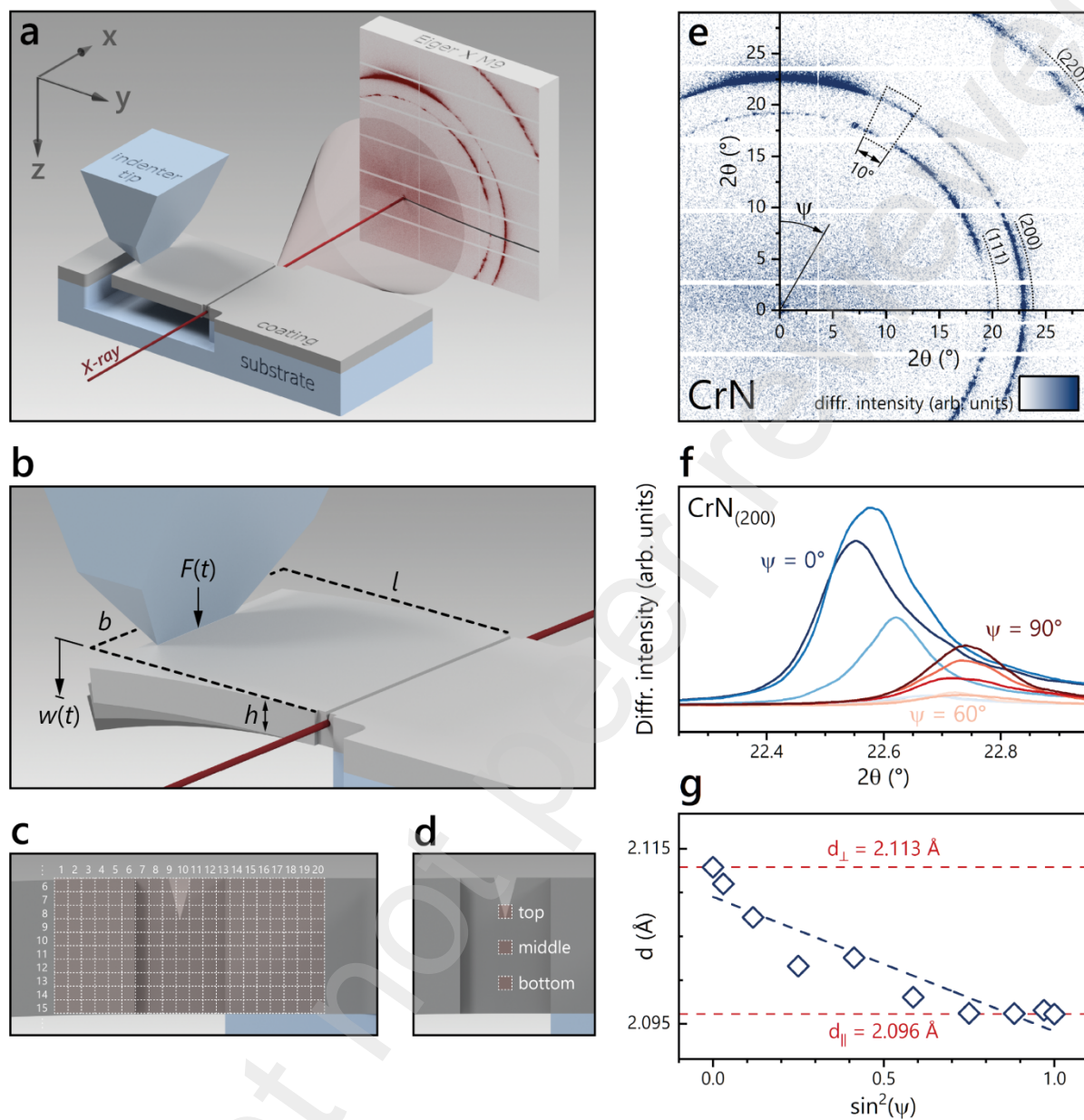
11

Figure 1 (double-column, color): (a) Schematic view of the *in situ* cross-sectional X-ray nanodiffraction setup. A $Cr_{0.94}N$ microcantilever sample with dimensions $25 \times 25 \times 3$ μm³ (length × width × height), cut from a substrate-coating lamella, was scanned with an X-ray beam obtaining a cross-section of ~250 nm. The microcantilever was loaded using a diamond wedge tip with a contact length of 10 μm, positioned at a distance of 23 μm from the pre-notch, and centered along the cantilever width. The 2D Debye-Scherrer diffraction patterns were recorded using an Eiger X M9 photon-counting detector. (b) Detail showing the geometry and deflection $w(t)$ of the microcantilever under a static and/or cyclic load $F(t)$, applied using the nanoindenter tip.

(c) During static loading, the X-ray beam was scanned along the *y*- and *z*-axis in steps of 300 nm creating a 20 × 20 grid centered around the pre-notch position, whereas during (d) cyclic loading, three positions along the cantilever height ("top", "middle", "bottom"; located at the pre-notch position in *y*-direction) were repeatedly scanned for the duration of the loading experiment. (e) Representative intensity plot of the recorded Debye-Scherrer patterns. The intensities of the (200)-peak were integrated in direction of the azimuthal angle ψ within 10° segments (dot-marked area) for ψ = 0 to 90° and (f) plotted as function of the diffraction angle. (g) Lattice parameters derived from the peaks plotted in (f) as function of $sin^2(\psi)$ including a corresponding linear fit for stress analysis.

2.4. Synchrotron X-ray nanodiffraction data analysis

The recorded 2D diffraction patterns were analyzed with respect to the phase evolution and the in-plane stress state $\sigma_\parallel$, both for static as well as dynamic loading conditions. To evaluate the stress state of the cantilever cross-section $\sigma_\parallel(y,z)$ an integration of the recorded patterns was performed in direction of the azimuthal angle ψ in segments of 10° from ψ = 0 to 90° (see Figure 1e). Within the so obtained radial intensity distributions $I(\theta,\psi)$ the positions of distinct diffraction peaks $2\theta(\psi)_{hkl}$ (*e.g.*, (200)-peak for CrN), and thus also the orientation-dependent lattice spacing $d(\psi)_{hkl}$, were determined by fitting a Pseudo-Voigt function to the spectrum (see Figure 1f and g). Subsequently, the orientation-dependent lattice strain $\varepsilon(\psi)_{hkl}$ was calculated following

$$\varepsilon_{hkl}(\psi) = \frac{d(\psi)_{hkl} - d_0(\psi^*)_{hkl}}{d_0(\psi^*)_{hkl}} \quad , \tag{5}$$

where $d_0(\psi^*)_{hkl}$ is the lattice spacing in the stress-free direction ψ_{hkl}^*, which itself is expressed by a set of X-ray diffraction elastic constants (XEC) $s_{1,hkl}$ and $\frac{1}{2}s_{2,hkl}$ in the form of

$$\sin(\psi_{hkl}^*) = \sqrt{\frac{-2s_{1,hkl}}{\frac{1}{2}s_{2,hkl}}} \quad . \tag{6}$$

13

Both the XEC were adopted from literature, *e.g.*, as $s_{1,hkl}^{CrN,(200)}$ = -0.3013 $\times$ 10^{-3} GPa^{-1} and $\frac{1}{2}s_{2,hkl}^{CrN,(200)}$ =

2.584 $\times$ 10^{-3} GPa^{-1} for CrN [52,53]. Following the *sin^2(ψ)*-method and the assumption of an elastically

isotropic material under a biaxial stress state the fundamental equation for the in-plane stress state

follows

$$\varepsilon_{hkl}(\psi) = \frac{1}{2}s_{2,hkl} \sigma_\parallel(y,z) \times \sin^2(\psi) + 2s_{1,hkl}\sigma_\parallel(y,z) \qquad . \qquad (7)$$

The described 2D pattern and data processing was conducted using the open-source software package

DPDAK [54] as well as a self-written MATLAB script [55] (The MathWorks Inc., version R2019b, Natick,

Massachusetts).

14

3. Results & Discussion

In the following, the results of the experimental work are presented and discussed thoroughly. Figure 2 shows a schematic overview of the entire coating synthesis and characterization workflow (Figure 2a-e), as well as exemplarily the material response during fracture and fatigue experiments (Figure 2f-j). In Section 2.1, the general framework of this study is established, outlining the materials selection and thin film properties with respect to phase formation, crystal structure, chemical composition, and apparent growth morphology (Figure 2a-b, f). This framework subsequently allows for closer insights into the fracture resistance (Figure 2c-left) and elasto-plastic deformation behavior (Figure 2d) of thin film materials under quasi-static loads, as discussed in Section 2.2. Therein, focused ion beam machining is used to produce free-standing microcantilever and micropillar specimen to determine the material specific fracture toughness (Figure 2g) and amenability to plastic deformation (Figure 2h), respectively. Taking the observed deformation mechanisms into account, the established knowledge is further developed towards dynamic loading conditions in Section 2.3. Performing cyclic cantilever bending experiments up to the high cycle fatigue regime (Figure 2c-right) provides details on the fatigue resistance of each coating material (Figure 2i), and highlights the correlation between the fatigue strength and fundamental material properties. In Section 2.4., the micromechanical fatigue experiment is coupled with a novel *in situ* synchrotron X-ray nanodiffraction setup (Figure 2e, j). Through this approach, the direct effect of imposing cyclic loads on larger cantilever structures is reviewed, revealing the cross-sectional stress distribution, phase evolution, and fatigue resistance of selected thin films.
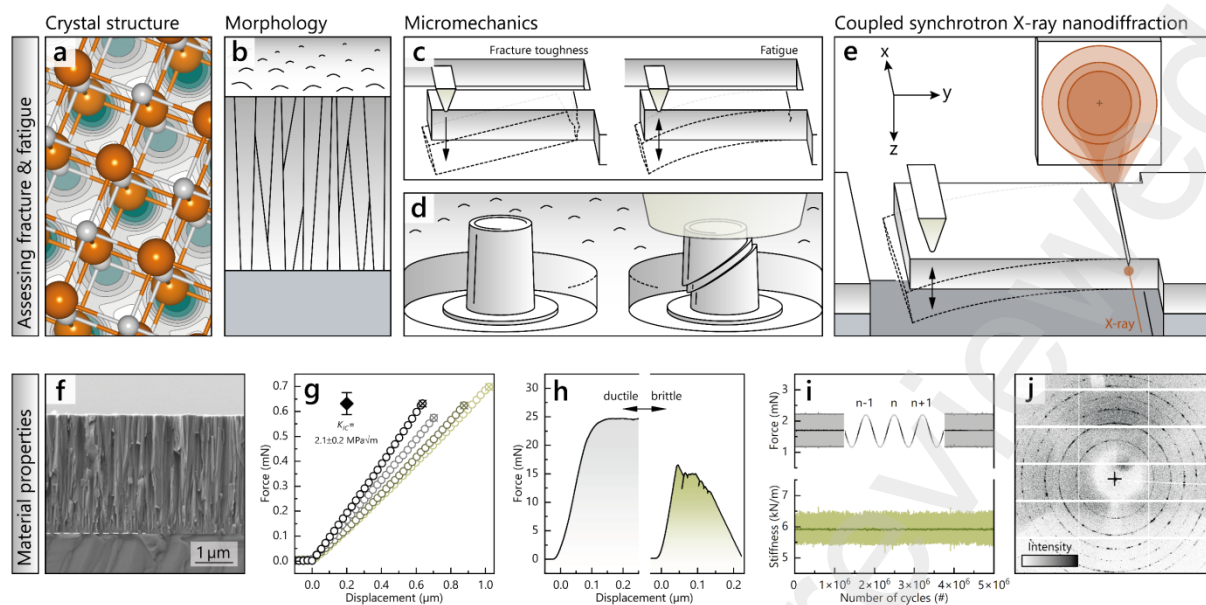
15

Figure 2 (double-column, color): Illustration showing the methodical approach to assess the fracture and fatigue resistance of thin films. (a-b) depict the fundamental thin film constitution in the form of the apparent crystal structure and growth morphology, respectively. (c) comprises microcantilever bending experiments to determine the coating fracture toughness (left) or the material response under prolonged cyclic loading (right). (e) shows the configuration for coupling *in situ* synchrotron X-ray nanodiffraction with cyclic bending experiments. Exemplary data obtained following the approach in (a-e) is further presented: (f) thin film fracture cross-section revealing the growth morphology of a Cr thin film; (g) force - displacement data obtained from fracture toughness experiments; (h) force - displacement data obtained from micropillar compression experiments indicating a ductile and brittle material response; (i) microcantilever stiffness and loading force data obtained from cyclic cantilever bending experiments; (j) diffraction pattern obtained from *in situ* synchrotron X-ray nanodiffraction.

3.1. Phase formation and growth morphology

The structural analysis of all Cr-based thin films obtained by X-ray diffraction is summarized in Figure 3. The diffractograms are arranged from bottom to top as metallic Cr (*bcc*, squares), $Cr_{0.94}N$ (*fcc,* circles), $Cr_{1.03}B_2$ (*hcp*$_{191}$, triangles), and $Cr_{1.79}O_3$ (*rh*, diamonds), respectively, and further complemented by the standardized 2θ reference peak positions [56–59]. The data clearly shows the phase-pure crystal

16

structure of all coatings, alongside an almost perfect stoichiometry for all Cr-based compounds with respect to their nominal composition. Moreover, all diffractograms indicate a polycrystalline, randomly oriented crystal growth except for $Cr_{1.03}B_2$, which obtains a clearly preferred orientation in the (001)-direction.
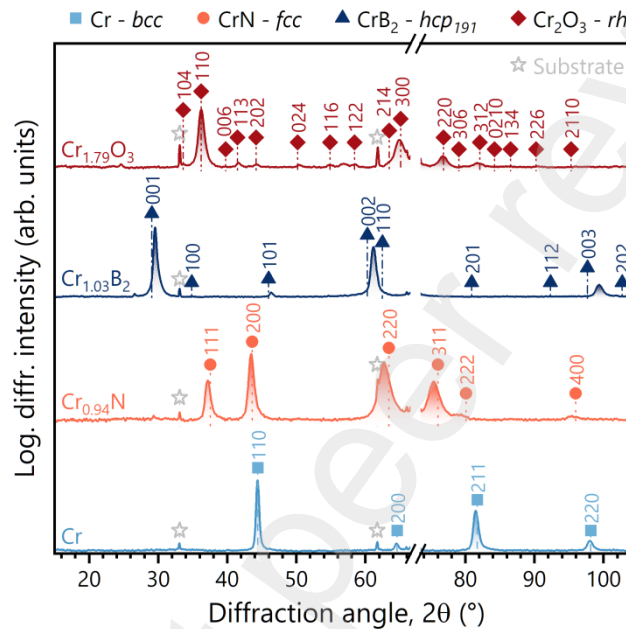

Figure 3 (single-column, color): XRD diffractograms of all Cr-based thin films measured on (100)-oriented silicon substrates (cubic, open star, [60]) including the corresponding 2θ peak positions of standardized reference patterns [56–59]. The diffractograms are arranged with metallic Cr (*bcc*, squares), $Cr_{0.94}N$ (*fcc,* circles), $Cr_{1.03}B_2$ (*hcp*[191], triangles), and $Cr_{1.79}O_3$ (*rh*, diamonds) from bottom to top, respectively.

All coatings were additionally investigated in more detail regarding their growth morphology and grain boundary constitution using cross-sectional SEM and top-view TEM, respectively. Figures 4a, c, e, and g depict the fracture cross-sections of single side coated silicon substrates, whereas Figures 4b, d, f, and h include the corresponding top-view TEM micrographs prepared from the identical specimen. All thin film materials obtain a dense, homogenous growth morphology over the entire coating thickness, which eventually concludes in a smooth top surface. Here, especially the thin films synthesized from

17

metallic Cr, $Cr_{0.94}N$ as well as $Cr_{1.79}O_3$ exhibit a pronounced formation of crystal columns, growing perpendicular to the coating-substrate interface. Typical for DCMS sputtered thin films, the columns appear to be interrupted and regularly forced to re-nucleate due to competitive crystal growth [61]. Contrary, $Cr_{1.03}B_2$ presents a rather featureless cross-section, lacking in clearly separated morphological features. These findings are largely supported by the corresponding bright-field TEM micrographs, presenting a dense and void-free growth structure for all coatings. Furthermore, the micrographs of metallic Cr and $Cr_{0.94}N$ especially highlight the individual crystal columns by a distinct orientation dependent contrast, whereas those for $Cr_{1.03}B_2$ and $Cr_{1.79}O_3$ obtain a slightly less pronounced visual separation. Using a line intercept method, the average crystal size was determined for all thin film materials. Within the analyzed volumes, the pure Cr thin film was evaluated with the largest crystal size of ~277 nm, followed by $Cr_{1.03}B_2$ with ~201 nm, and then $Cr_{0.94}N$ as well as $Cr_{1.79}O_3$ with ~143 and 123 nm, respectively. These results suggest that the coatings synthesized in pure Argon atmosphere tend to form larger crystals, whereas both coatings sputtered in reactive environment are subject to enhanced re-nucleation and thus obtain slightly smaller grains. The TEM micrographs allowed for further microstructural analysis of the grain-boundary constitution. Here, the absence of distinct grain-boundary phases was confirmed, which is in line with the exact stoichiometry obtained for all Cr-based coatings and the results received during XRD analysis.

The here presented results outline the framework for all subsequent fracture and cyclic loading experiments. Considering that the ensemble of synthesized coatings shows a vastly comparable thin film structure, the observed material properties will be particularly connected to the apparent bonding nature of the individual thin film [62]. This is considered as an essential aspect for elucidating possible origins for varying fracture and fatigue characteristics.
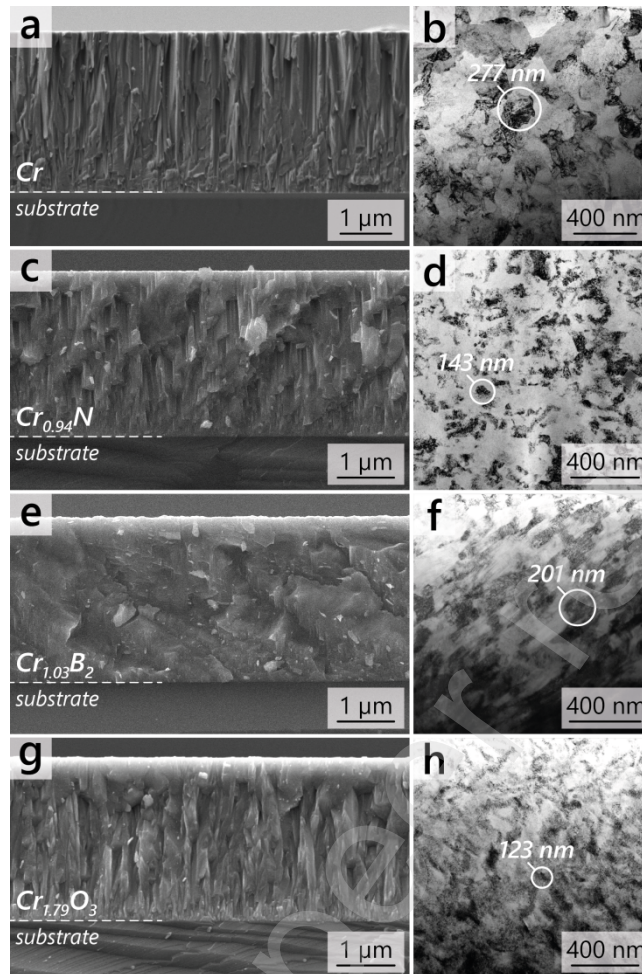
18

Figure 4 (single-column, color): (a), (c), (e), and (g) show SEM fracture cross-sections of all Cr-based thin films deposited on (100)-oriented silicon substrates. (b), (d), (f), and (h) present corresponding top-view bright-field TEM micrographs including the average crystallite grain size of the film cross-sections depicted in (a), (c), (e), and (g).

3.2. Fracture characteristics

Micromechanical bending experiments on all four coating materials reveal a pronounced variation in the fracture resistance as depicted by the raw indenter force-displacement curves shown in Figure 5a. In addition, Figure 5b presents the data normalized in terms of stress intensity and bending strain. The results show that $Cr_{1.03}B_2$ obtains the highest critical fracture force during micro cantilever bending tests at $F_C \sim 810\pm65$ µN. Consequently, this also translates into the highest calculated fracture

19

toughness with K_{IC} ~ 4.3±0.3 MPa√m. Compared to previous studies reporting on the fracture toughness of nitride-based thin films, this material system appears to outperform many industrially relevant coatings such as Ti-Si-N or α-Al$_2$O$_3$ [63,64]. In contrast, the data recorded for Cr$_{0.94}$N and Cr$_{1.79}$O$_3$ indicates drastically lower critical fracture loads of F_C ~ 332±14 and 232±22 µN, thus resulting in fracture toughness values of K_{IC} ~ 2.1±0.1 and 1.6±0.2 MPa√m, respectively. Surprisingly, the values obtained for the metallic Cr coating are located in between these boundaries, obtaining a critical fracture force of F_C ~ 462±31 µN and a corresponding fracture toughness of K_{IC} ~ 3.6±0.3 MPa√m. Here, it is essential to note that the metallic material is particularly prone to dislocation motion and hence plastic deformation, which manifests in a slight curvature of the load - displacement curve prior to the ultimate fracture- or yield-point (see Figure 5a). This, however, stands in partial violation of the testing conditions outlined within the frameworks of linear elastic fracture mechanics (LEFM). Consequently, the fracture toughness values for the Cr thin film should be treated carefully, especially when compared to results deduced from different procedures. Nevertheless, results for the metallic Cr were expected to considerably exceed those obtained for the ceramic thin films, irrespective of the known brittleness to the body-centered cubic crystal structure below the ductile-to-brittle transition temperature [65].

Upon specifically regarding the elastic deformability of the thin films, all Cr-based compounds show a comparable maximum bending strain in the range of ε = 1-1.2 %, whereas the metallic coating exhibits an extended displacement up to w > 1.5 µm and ε > 1.5 % prior to failure. This is especially interesting when considering the absence of elastic differences as obtained from instrumented nanoindentation experiments, where an almost identical Young's modulus of E ~ 310 GPa was determined for all investigated coatings (see Table 1 in the Experimental Section). These observations eventually raise several intriguing questions: What are possible origins for the marked difference in fracture toughness of the coating materials? Is there a particular connection to (intrinsic) toughening mechanism that hinder crack propagation?
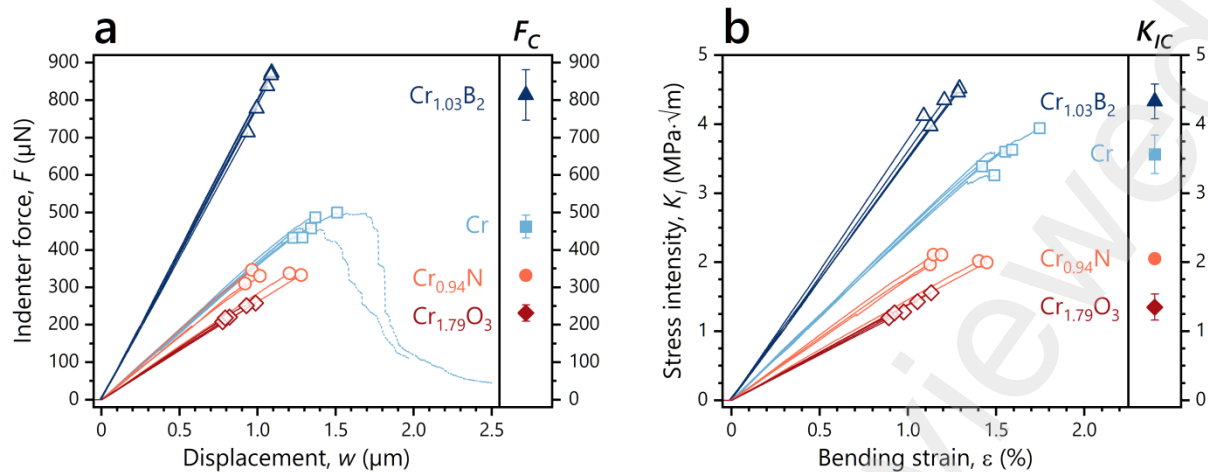
20

Figure 5 (double-column, color): (a) Indenter force - displacement curves of all Cr-based thin films recorded during *in situ* bending experiments on free-standing microcantilever geometries. Critical fracture loads and deflections are indicated using the material corresponding symbols introduced in Figure 3. The mean value and standard deviation of the critical fracture load is included for each thin film on the right axis. (b) Normalized stress intensity - bending strain curves calculated from the data in (a) and post-mortem analysis of the individual geometry of each fractured cantilever cross-section. Critical stress intensities and bending strains, as well as mean values for the apparent fracture toughness of all thin films, are again included analogous to (a).

Assuming morphological consistency between the thin films, a primary connection can be drawn to the apparent bonding structure and strength of each material (*i.e.*, metallic, covalent, ionic, or a combination thereof). In principle, any fracture process ultimately involves the rupture of interatomic bonds – occurring on intra-crystalline lattice planes or generic grain boundary sites. Thus, the stronger the bonds, the higher the resistance against fracture. This holds particularly true for brittle fracture processes, which are entirely determined by atomistic events at the crack tip location [66]. However, also increasing the ductile character in generally brittle ceramic thin films by tailoring the fraction of metallic bonds was shown to enhance the fracture resistance by enabling intrinsic toughening mechanisms (*e.g.*, crack-tip blunting) [67,68]. Specifically, within the Cr-based compounds, the atoms are bound by a mixture of strong covalent, ionic, and metallic bonds, as such they are less ductile compared to pure Cr, which is predominantly characterized by the latter type. Nevertheless, especially

21

CrB$_2$ may possess a significant ductile character – in combination with a strong, covalently bound 2D boron network [69] – thus explaining the high fracture toughness value. Quantitatively grasping these differences in bond strength is, however, extremely difficult. Though at this point, the authors would like to add that density-function-theory (DFT)-based techniques do provide a general classification of bonding models – *i.e.*, by calculating the density of states (DOS) or the crystal orbital Hamilton population (COHP) [70]. In this work, a descriptive approach using micropillar compression experiments is selected to further elucidate the bond structure variation and to obtain a qualitative insight, especially on the plastic deformation response of all Cr-based materials.

Therefore, engineering stress (σ_{eng}) vs. compressive strain (ε_{comp}) curves from uniaxial compression tests of micropillars prepared from all Cr-based thin films are summarized in Figure 6. Regarding the calculated yield strengths (see Figure 6, left column), strong similarities were found with the fracture limits depicted in Figures 5. Although the materials were stressed in the opposite regime, the material response showed that Cr$_{1.03}$B$_2$ again obtains the highest yield strength at σ_y ~ 8.9±0.5 GPa, followed by Cr$_{0.94}$N and Cr$_{1.79}$O$_3$ with values of σ_y ~ 6.0±0.4 and 4.0±0.1 GPa, respectively. Related to the pure metallic bonding character of the Cr thin film, the lowest yield strength with σ_y ~ 2.4±0.1 GPa was observed, which is in excellent agreement with previous values obtained for nanocrystalline bulk Cr [71]. Moreover, the compression tests reveal vastly different stress-strain responses past the yield point, from which varying "levels" of plasticity can be deduced. Most prominent, both Cr and Cr$_{1.03}$B$_2$ show very similar behavior, with extensive plastic flow upon reaching σ_y (see Figure 6, center column). Moreover, Cr even shows a tendency towards steady rate work hardening [13]. Contrary, Cr$_{0.94}$N and Cr$_{1.79}$O$_3$ pillars exhibit a strongly brittle behavior, being characterized by discrete strain burst events and a lack of deformation stability (see Figure 6, right column). In fact, this behavior is seen in the absence of active deformation mechanisms due to the high energy barrier preventing dislocation motion, consequently impeding continuous plastic deformation [72]. In this sense, the here calculated yield strength can also be referred to as the compressive strength of both materials. These results not only confirm the suggested accessibility of plastic flow within nanostructured Cr and Cr$_{1.03}$B$_2$ thin films

22

but also span a clear connection between the intrinsic bonding character and the apparent fracture resistance for the loading conditions shown.
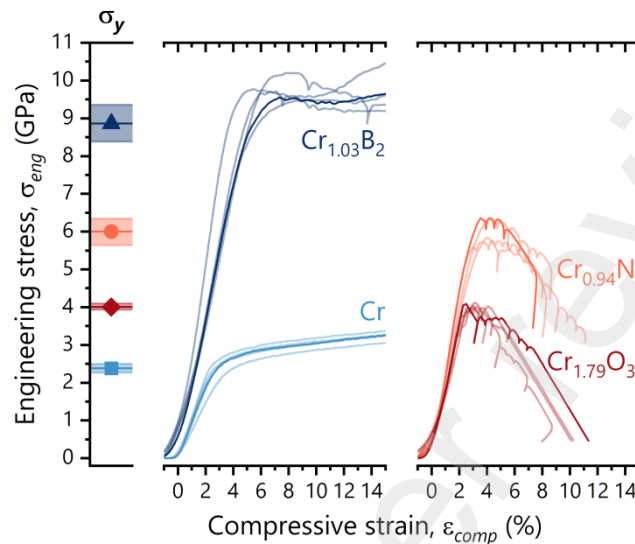

Figure 6 (single-column, color): Engineering stress - compressive strain curves of all Cr-based thin films recorded during *in situ* micropillar compression experiments. The data is arranged according to the predominant material response, hence results for Cr and $Cr_{1.03}B_2$ are merged in the center section, whereas the results for $Cr_{0.94}N$ and $Cr_{1.79}O_3$ are included in the right-hand section. Note the extended plastic deformation of Cr and $Cr_{1.03}B_2$ after reaching the yield point, contrary $Cr_{0.94}N$ and $Cr_{1.79}O_3$ are characterized by consecutive strain burst events and a lack of deformation stability. The mean value and standard deviation of the yield stress are included for each thin film in the left-hand section.

3.3. Fatigue characteristics

To further develop the established picture of the mechanical response of all Cr-based thin films towards dynamic loading conditions, *in situ* cyclic cantilever bending tests were performed. Here, an identical setup as used during the fracture toughness experiments was employed, except the applied force being oscillated at a frequency of f = 500 Hz between 60 and 90 % of the material specific critical fracture limit (see Figure 5). A representative evolution of the indenter force is depicted as a function

23

of the number of load cycles for the $Cr_{0.94}N$ specimen in Figure 7a. The recorded data gives the continuous force application onto the micro cantilever, comprised of a mean force (dark blue line) overlaid with a sinusoidal amplitude force (light blue area around the mean force) up to $n = 10^7$ cycles (see Figures 7a and b). Examining the cantilever stiffness evolution showed a very alike behavior for all Cr-based materials, given that the initial stiffness values were preserved throughout the entire loading duration (see Figure 7c). Contrary, any crack propagation occurring would result in a drastic reduction of the cross-sectional area, in turn showing a decrease of the recorded stiffness. Considering that the applied loads approached the instantaneous fracture threshold, the displayed mechanical response closely resembles that observed for highly brittle materials. There, active and stable crack growth is typically confined to a narrow range in terms of the stress intensity, below which pre-existing cracks are considered dormant, while above rapid failure occurs [6,7,73]. Moreover, crack formation is invariably associated with activating these pre-existing flaws rather than a natural initiation related to dislocation glide. Nevertheless, the non-existent crack extension and preserved endurance strength of as high as 90 % of the respective single cycle strength (*i.e.*, the fracture toughness) – maintained well within the high cycle fatigue (HCF) regime – are distinct from typical bulk material behavior. These findings are especially striking when considering the pre-notch at the fixed end of the cantilever, serving as stress concentration and possible crack nucleation site. Interestingly, also the metallic Cr coating follows this tendency, despite the metallic bond structure and previously observed plasticity under quasi-static loading conditions (see Figures 5 and 6). However, as mentioned in the opening section of this work, recent studies on the fatigue behavior of metallic thin films such as copper showed a length-scale dependent transition of the active fatigue mechanisms. In fact, decreasing the characteristic microstructural dimensions to the nanometer regime imposes growing constraints on dislocation activities – necessary to form extrusions or intrusion – resulting in a pure crack dominated fatigue mechanism, analogous to that of brittle ceramic materials [8,27].
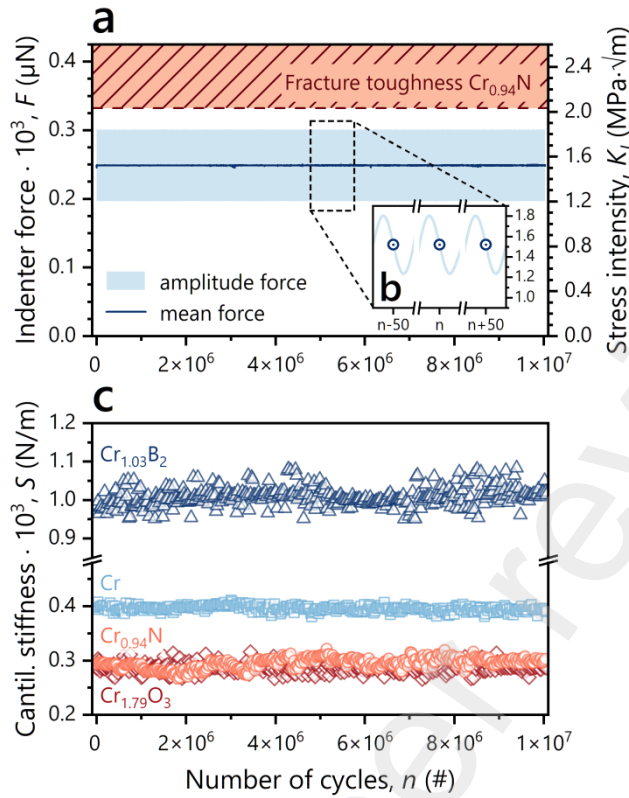
24

Figure 7 (single-column, color): (a) Representative indenter force (left axis) vs. load cycle evolution recorded during cyclic loading of a free-standing microcantilever prepared from a Cr-based thin film (here $Cr_{0.94}N$). The applied stress intensity, including the reference fracture toughness determined in Figure 5b, is included on the right axis. (b) Schematic detail of the load evolution showing the continuous force application on the micro-cantilever as well as individual data points recorded every 50th load cycles. (c) Corresponding cantilever stiffness - load cycle evolution for all Cr-based thin films (material corresponding symbols apply according to Figure 3).

The general picture that emerges from the fatigue tests on all Cr-based thin films suggests that the applied loads and cycle numbers exclusively trigger an elastic material response without causing any noticeable material damage. In turn, this suggests that the actual fatigue resistance or endurance strength of such nanostructured coating materials is primarily defined and limited by the intrinsic fracture toughness – a material property closely related to the prevalent bonding character. Hence, upon eliminating the influence of a substrate-coating interface, the fatigue strength is given when the following condition holds true:

$$K_I \leq K_{IC} \quad . \tag{8}$$

25

3.4. Coupled synchrotron X-ray nanodiffraction and fatigue experiments

A more elaborate, detailed understanding of this observed material response from the aspect of intrinsic stress distributions and local phase formation was obtained by coupling the fatigue experiments with synchrotron X-ray nanodiffraction. Using this *in situ* synchrotron X-ray nanodiffraction setup, the phase evolution and stress state of larger micro-cantilever specimen was studied around the notch area in both the as-fabricated as well as under static (see Figure 1c) and dynamic loading conditions (see Figure 1d). These experiments aimed to correlate the observed fracture behavior and absence of fatigue induced damage with the intrinsic properties of the tested thin film materials.

A representative stress distribution around the pre-notch position, calculated according to the procedure described in Figures 1e-g, is shown in Figure 8 for a cantilever produced from the $Cr_{0.94}N$ coating. Figure 8a presents the in-plane stress distribution in the as-fabricated state (K_I = 0 % of K_{IC}*), exhibiting a uniform compressive stress distribution of $\sigma_\parallel (y,z)$ ~ -2.1 GPa. K_{IC}* equals the reference fracture toughness of the cantilever specimen – for further details see the Experimental Section. At first glance, these data suggest that the residual stress is closely associated with the apparent film growth kinetics during PVD synthesis, leading to the visualized compressive stress state. However, considering the free-standing end of the micro-cantilever and the removal of substrate material constraints, this calculated in-plane stress map is in violation of the force and momentum equilibrium for the coating cross-section. In fact, given by the uniform appearance of the stress distribution, the area surrounding the pre-notch position should be rather interpreted as stress free, with the data corrected by shifting the mean value of $\sigma_\parallel (y,z)$ to 0 GPa. This offset is understood as an artifact of the experimental setup and prevailing X-ray beam conditions. Moreover, these results also imply homogeneous growth conditions since the deduced data presents no stress gradients across the entire coating thickness.
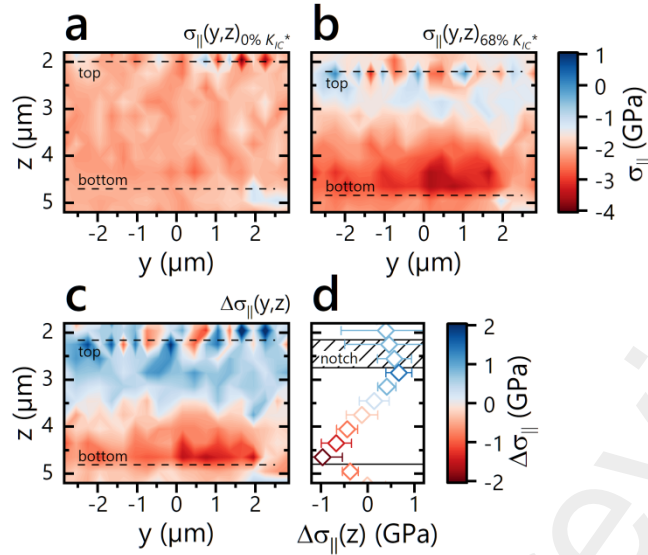
26

Figure 8 (single-column, color): In-plane stress map of a $Cr_{0.94}N$ cantilever around the pre-notch position (y = 0) in the (a) unloaded and (b) loaded state (stress intensity equals 68 % of the reference fracture toughness K_{IC}*). Note the uniform compressive stress state in (a) violates the equilibrium condition and is attributed to a consistent measurement artifact throughout all diffraction experiments. (c) Corresponding delta map showing the difference between the stress states depicted in (a) and (b), including the (d) cross-sectional row-average of the data in (c). The top and bottom surface of the cantilever as well as the notch depth are indicated as guidance in all figures.

Upon loading the cantilever to K_I = 68 % of K_{IC}* (see Figure 8b), which closely resembles the mean stress intensity applied during subsequent fatigue experiments, the upper segment depicts an expected reduction in the compressive stress state, while the bottom segment shows a proportional increase. The applied stress intensity is referenced to the actual K_{IC}* value of the examined cantilever sample, determined after recording the static stress map. In order to compensate for the stress data offset identified in Figure 8a, both stress distributions are subtracted to yield the relative change in the in-plane stress state $\Delta\sigma_{\parallel}(y,z)$ (*i.e.*, the apparent stress during bending), which is presented in Figure 8c as well as in Figure 8d in the form of a cross-sectional average. Applying load onto the cantilever is shown to cause a perfectly linear change of the in-plane stress over the cantilever cross-section, with the neutral axis centered along the height. The maximum stress change occurs on the upper and lower segments, with $\Delta\sigma_{\parallel}(z)_{max}$ ~ ±1 GPa for the given load. However, the stresses in the

27

upper-most part of the cantilever – approximately to a depth of the pre-notch – deviate from this linear behavior, instead an almost constant tensile stress of $\Delta\sigma_\parallel(z) \sim 0.5\text{-}0.6$ GPa is observed. In accordance with Ref. [48], this could be explained by the strain relief on the cantilever surface introduced by the pre-notch (note the through-thickness type notch), which locally reduces the tensile stress component imposed by the bending moment. Consequently, this shifts the maximum tensile stress to the tip of the pre-notch. Yet, despite the small X-ray probe diameter of ~250 nm, the local stress concentration occurring close to the pre-notch tip could not be resolved within the accuracy of this method. Nevertheless, the bottom surface of the loaded cantilever obtains a distinct compressive stress region with $\Delta\sigma_\parallel(y,4.75)$ values exceeding -4 GPa ($\triangleq$ -1.9 GPa after correction) within y = 0 - 1 µm (see Figure 8b), confirming the stress concentration introduced by the pre-notch.

Knowing the actual stress distribution during the bending experiments, additional fatigue tests were conducted on these large cantilever specimens. Coupled with the cyclic loading, three distinct positions across the cantilever height were probed (see Figure 1d) using the *in situ* X-ray nanodiffraction setup to resolve the structural and stress state evolution. Figure 9a exemplarily depicts the results obtained for the $Cr_{0.94}N$ coating, showing the applied indenter force (left axis) as a function of the number of load cycles and an additional reference in terms of the critical stress intensity (right axis). The cantilever was stressed in a range of K_I = 48 - 83 % of $K_{IC}*$ for a total duration of $n = 5 \times 10^6$ cycles. The recorded response of the cantilever stiffness (see Figure 9b) was, analogous to the previous observations in Figure 7c, maintained throughout the experiment at $S \sim 2680$ N/m. This value is linearly proportional to the stiffness recorded for the smaller cantilever and scales with the sample width. Hence, despite the larger specimen size and consequently an increased probability for pre-existing critical flaws – apart from the pre-notch – no fatigue induced damage was observed. This was additionally confirmed by measuring the apparent fracture toughness of the examined cantilever, where a value of $K_{IC}*$ = 1.1 MPa√m was calculated, matching the previously established reference (see Figure 9a; note, $K_{IC}*$ serves as a reference within this work, the actual value is however calculated outside the geometrical boundaries given in Ref. [15]).
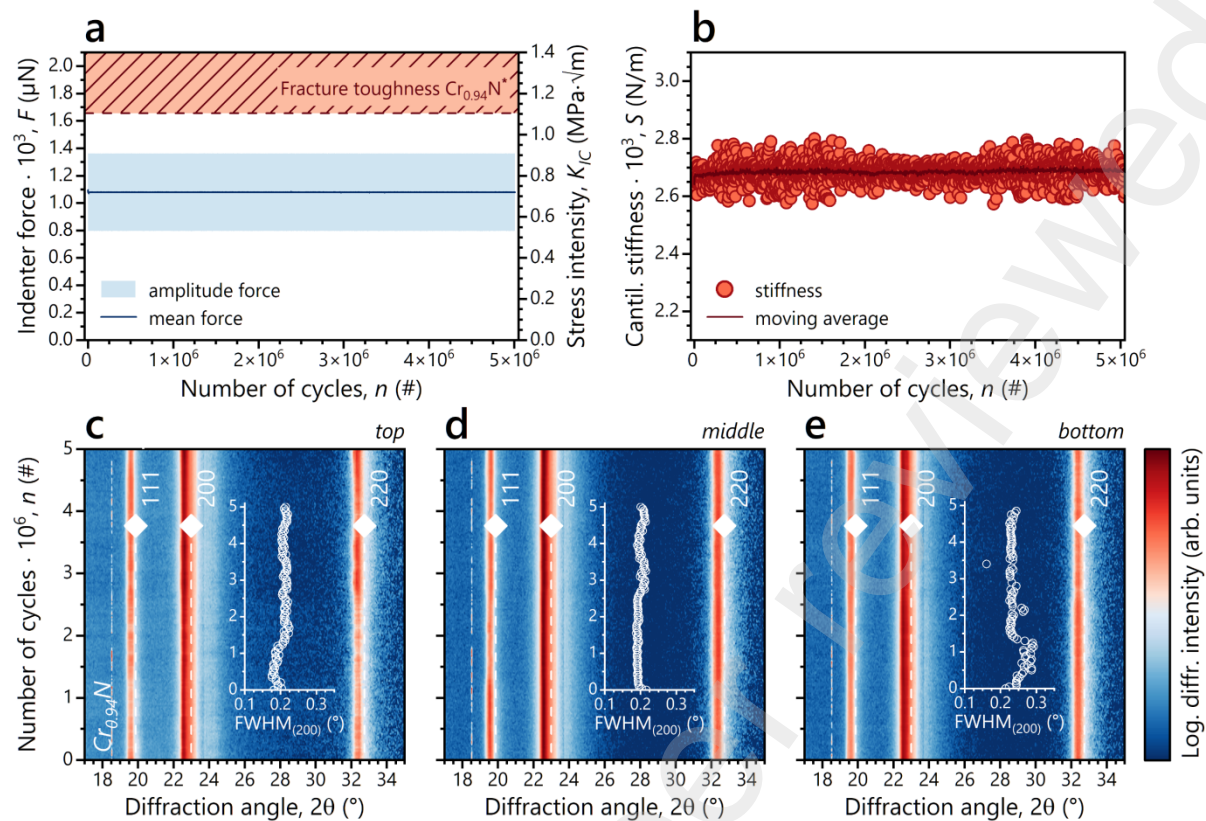
28

Figure 9 (double-column, color): (a) Representative indenter force (left axis) vs. load cycle evolution recorded during cyclic loading of a microcantilever prepared from a Cr-based thin film (here $Cr_{0.94}N$). The applied stress intensity, including the fracture toughness threshold $K_{IC}*$ determined during pre-testing on identical cantilever samples, are included on the right axis. (b) Corresponding cantilever stiffness - load cycle evolution, including a moving average fit. (e - g) Intensity plots from *in situ* X-ray nanodiffraction experiments depicting the phase evolution of a $Cr_{0.94}N$ microcantilever over 5×10^6 load cycles for the measurement positions defined in Figure 1d, respectively. The individual diffractographs are derived from azimuthal integration of the recorded Debye-Scherrer ring patterns. All intensity plots contain insets depicting the evolution of the FWHM of the (200)-peak as a function of the number of cycles.

The associated X-ray intensity plots are summarized in Figures 9c-e, showing the azimuthally integrated Debye-Scherrer patterns as function of the diffraction angle and number of load cycles. Correlating the structural evolution with a standardized reference pattern of face-centered cubic CrN [57] illustrates that no change in the apparent crystal structure occurs as consequence of the

29

applied mechanical stress. Moreover, the observed diffraction maxima are consistently shifted towards lower 2θ angles on all cross-sectional positions, which is associated with the minute chemical differences between the reference structure and the sample in question.

Looking more closely at the shape and intensity of the recorded diffractographs, the full width at half maximum (FWHM) was quantified for the (200)-peak as function of the load cycles (see inserts in Figures 9c-e). The results display a slightly increasing average value for the FWHM from positions "top" (~0.20°) to "bottom" (~0.23°), which is due to incorporating the primary nucleation front at the former substrate-coating interface into the X-ray gauge volume. Additionally, upon assuming stability of the coherently diffracting domains – in contrast to the mechanically induced grain growth observed for *fcc*-structured metal thin films [74] – the FWHM suggests that the initial stress state is preserved in all measurement positions. Altering the stress distribution, both towards tensile or compressive, would result in a distortion of the Debye-Scherrer ring pattern and a changed peak shape when fully integrating the diffracted intensity in azimuthal direction. Specifically verifying the stress distribution at $n = 3 \times 10^6$ load cycles (see Figure 10a and b, red circles) assumes similar values as observed for static loading conditions in $\Delta\sigma_{\parallel}(0,z)$ of Figures 8c and d. An increased compressive stress of ~ -1.5 GPa is calculated on the cantilever bottom, while the neutral axis and top surface roughly remain in their initial stress-free condition (blue diamonds, determined as cross-sectional average of Figure 8a). Again, the absence of an increasing tensile stress in the "top" position is associated with the strain relieve introduced by the pre-notch. Furthermore, it is important to mention that the calculated stress values correspond to an averaged load state, since the associated Debye-Scherrer diffraction patterns were recorded over ~5000 load cycles each.

Finally, during the first 10^6 load cycles, both the FWHM on the cantilever top and bottom show an opposite behavior by noticeably increasing or decreasing from their initial values, respectively, while the center position remains unchanged. Here, one may speculate a running-in phase where microplasticity at local stress concentrations (*i.e.*, defect sites, column boundaries, etc.) allows for a change in the coherently diffracting domains. Nevertheless, the definite origin of this behavior remains

30

questionable, especially considering that no such change can be observed in the cantilever stiffness during the timeframe.

In summary, the coupled *in situ* synchrotron X-ray nanodiffraction and fatigue experiments confirm the limiting aspect of the fracture toughness on the fatigue strength of our nanostructure thin film materials (see Equation 8). Moreover, the recorded in-plane stress state and phase evolution for $Cr_{0.94}N$ underline the purely elastic material response during the cyclic bending experiments despite the load amplitudes closely approaching the critical stress intensity threshold.
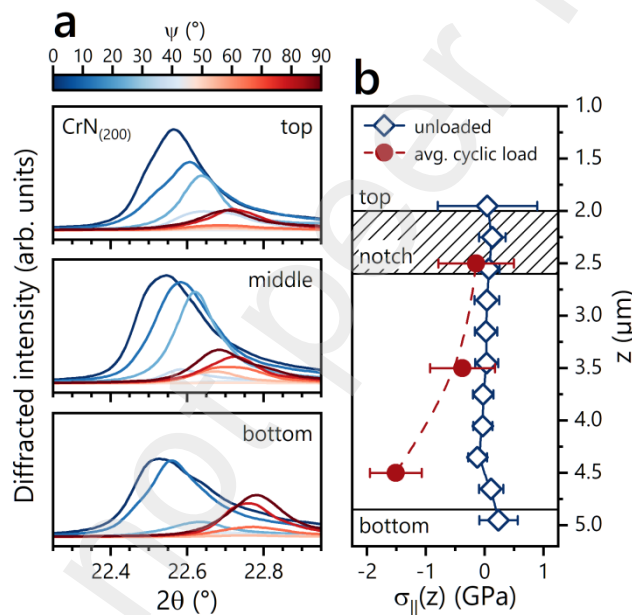

Figure 9 (single-column, color): (a) Diffraction intensities of $Cr_{0.94}N$ for all measurement positions defined in Figure 1d, acquired during *in situ* nanodiffraction experiments. The data was calculated from the (200)-peak of the Debye-Scherrer ring patterns recorded at $n = 3 \times 10^6$ load cycles as described in Figures 1e-f. (b) Comparison of the stress distribution over the cantilever cross-section at the pre-notch position (y = 0) between the unloaded (blue diamonds; corrected row-average of the data included in Figure 8a) and the average loaded state (red circles) during cyclic bending of the microcantilever geometry. Each Debye-Scherrer ring pattern was acquired with an exposure time of 10 s; hence the latter stress state is averaged over 5000 load cycles. All stress data is corrected to meet the equilibrium condition according to Figure 8a.

31

4. Conclusion

This work presents a systematic approach towards unraveling the fracture and fatigue properties of PVD deposited thin films by identifying the key aspects determining their durability under prolonged unidirectional loading. A novel *in situ* synchrotron nanodiffraction setup was developed in combination with micro-cantilever bending tests to determine the fracture toughness and fatigue resistance of a model material system comprised of sputter deposited Cr and Cr-based compounds (*i.e.*, CrN, CrB_2, and Cr_2O_3). This material selection permits valuable insights into the deformation mechanisms available with respect to the prevalent bonding nature and crystal structure. Given the morphological consistency of the examined materials – as confirmed by SEM and TEM investigations – a large divergence in the fracture toughness was observed, with values ranging from 4.3±0.3 down to 1.6±0.2 MPaVm for CrB_2 and Cr_2O_3, respectively. The apparent difference in the fracture resistance is further elucidated using micro-pillar compression tests, thereby spanning a clear connection between the intrinsic bonding character, prevalent crystal structure, and the accessible deformation mechanisms within each material. Discussed from this bonding nature inspired viewpoint, it could be demonstrated that the apparent fatigue strength of these nanostructured coatings is solely limited by the fracture toughness. Provided the condition $K_I \leq K_{IC}$ holds true during fatigue testing, all materials showed a purely elastic material response, so that cyclic bending tests up to $n = 10^7$ cycles were realized without any noticeable material damage, structural change, or shift in the cross-sectional stress distribution. Thus, on the basis of these observations, we propose that improving the intrinsic fracture toughness of nanostructured thin film materials is a pathway to facilitate enhanced fatigue strengths.

Acknowledgments

Data Availability Statement

The data that support the findings of this study are available from the corresponding author upon reasonable request.

Declaration of Interest Statement

The authors declare that they have no known competing financial interests or personal relationships that could have appeared to influence the work reported in this paper.

33

Bibliography

[1]   P. Cavaliere, Fatigue and Fracture of Nanostructured Materials, Springer International Publishing, Cham, 2021. doi:10.1007/978-3-030-58088-9.

[2]   S. Suresh, Fatigue of Materials, Cambridge University Press, 1998. doi:10.1017/CBO9780511806575.

[3]   C. Kirchlechner, P.J. Imrich, W. Liegl, J. Pörnbacher, J.-S. Micha, O. Ulrich, C. Motz, On the reversibility of dislocation slip during small scale low cycle fatigue, Acta Mater. 94 (2015) 69–77. doi:10.1016/j.actamat.2015.04.029.

[4]   H. Mughrabi, Cyclic slip irreversibilities and the evolution of fatigue damage, Metall. Mater. Trans. B Process Metall. Mater. Process. Sci. 40 (2009) 431–453. doi:10.1007/s11663-009-9240-4.

[5]   S. Lavenstein, Y. Gu, D. Madisetti, J.A. El-Awady, The heterogeneity of persistent slip band nucleation and evolution in metals at the micrometer scale, Science (80-.). 370 (2020). doi:10.1126/science.abb2690.

[6]   R.O. Ritchie, Mechanisms of fatigue-crack propagation in ductile and brittle solids, 1999. doi:10.1023/A:1018655917051.

[7]   R.O. Ritchie, R.H. Dauskardt, Cyclic fatigue of ceramics. A fracture mechanics approach to subcritical crack growth and life prediction, Nippon Seramikkusu Kyokai Gakujutsu Ronbunshi/Journal Ceram. Soc. Japan. 99 (1991) 1047–1062. doi:10.2109/jcersj.99.1047.

[8]   G.P. Zhang, C.A. Volkert, R. Schwaiger, P. Wellner, E. Arzt, O. Kraft, Length-scale-controlled fatigue mechanisms in thin copper films, Acta Mater. 54 (2006) 3127–3139. doi:10.1016/j.actamat.2006.03.013.

[9]   O. Kraft, P.A. Gruber, R. Mönig, D. Weygand, Plasticity in confined dimensions, Annu. Rev. Mater. Res. 40 (2010) 293–317. doi:10.1146/annurev-matsci-082908-145409.

[10]   R. Schwaiger, O. Kraft, Size effects in the fatigue behavior of thin Ag films, Acta Mater. 51 (2003) 195–206. doi:10.1016/S1359-6454(02)00391-9.

[11]   R. Pippan, S. Wurster, D. Kiener, Fracture mechanics of micro samples: Fundamental considerations, Mater. Des. 159 (2018) 252–267. doi:10.1016/j.matdes.2018.09.004.

[12]   G. Dehm, C. Motz, C. Scheu, H. Clemens, P.H. Mayrhofer, C. Mitterer, Mechanical Size-Effects in Miniaturized and Bulk Materials, Adv. Eng. Mater. 8 (2006) 1033–1045. doi:10.1002/adem.200600153.

[13]   M.D. Uchic, D.M. Dimiduk, J.N. Florando, W.D. Nix, Sample Dimensions Influence Strength and Crystal Plasticity, Science (80-.). 305 (2004) 986–989. doi:10.1126/science.1098993.

[14]   C.J. Szczepanski, S.K. Jha, P.A. Shade, R. Wheeler, J.M. Larsen, Demonstration of an in situ microscale fatigue testing technique on a titanium alloy, Int. J. Fatigue. 57 (2013)

131–139. doi:10.1016/j.ijfatigue.2012.08.008.

[15] K. Matoy, H. Schönherr, T. Detzel, T. Schöberl, R. Pippan, C. Motz, G. Dehm, A comparative micro-cantilever study of the mechanical behavior of silicon based passivation films, Thin Solid Films. 518 (2009) 247–256. doi:10.1016/j.tsf.2009.07.143.

[16] J.P. Best, J. Zechner, J.M. Wheeler, R. Schoeppner, M. Morstein, J. Michler, Small-scale fracture toughness of ceramic thin films: the effects of specimen geometry, ion beam notching and high temperature on chromium nitride toughness evaluation, Philos. Mag. 96 (2016) 3552–3569. doi:10.1080/14786435.2016.1223891.

[17] C. Kainz, M. Pohler, G.C. Gruber, M. Tkadletz, A.S. Ebner, C. Czettl, N. Schalk, Influence of bias voltage on microstructure, mechanical properties and thermal stability of arc evaporated Cr0.74Ta0.26N coatings, Surf. Coatings Technol. 417 (2021) 127212. doi:10.1016/j.surfcoat.2021.127212.

[18] R. Soler, S. Gleich, C. Kirchlechner, C. Scheu, J.M. Schneider, G. Dehm, Fracture toughness of Mo2BC thin films: Intrinsic toughness versus system toughening, Mater. Des. 154 (2018) 20–27. doi:10.1016/J.MATDES.2018.05.015.

[19] R. Hahn, N. Koutná, T. Wójcik, A. Davydok, S. Kolozsvári, C. Krywka, D. Holec, M. Bartosik, P.H. Mayrhofer, Mechanistic study of superlattice-enabled high toughness and hardness in MoN/TaN coatings, Commun. Mater. 1 (2020) 62. doi:10.1038/s43246-020-00064-4.

[20] I. El Azhari, J. Garcia, M. Zamanzade, F. Soldera, C. Pauly, L. Llanes, F. Mücklich, Investigations on micro-mechanical properties of polycrystalline Ti(C,N) and Zr(C,N) coatings, Acta Mater. 149 (2018) 364–376. doi:10.1016/j.actamat.2018.02.053.

[21] T. Csanádi, J. Wehrs, S. Grasso, M. Reece, J. Michler, J. Dusza, Anomalous slip of ZrB 2 ceramic grains during in-situ micropillar compression up to 500 °C, Int. J. Refract. Met. Hard Mater. 80 (2019) 270–276. doi:10.1016/j.ijrmhm.2019.01.021.

[22] T. Glechner, R. Hahn, T. Wojcik, D. Holec, S. Kolozsvári, H. Zaid, S. Kodambaka, P.H. Mayrhofer, H. Riedl, Assessment of ductile character in superhard Ta-C-N thin films, Acta Mater. 179 (2019) 17–25. doi:10.1016/j.actamat.2019.08.015.

[23] X.-M. Luo, B. Zhang, G.-P. Zhang, Fatigue of metals at nanoscale: Metal thin films and conductive interconnects for flexible device application, Nano Mater. Sci. 1 (2019) 198–207. doi:10.1016/j.nanoms.2019.02.003.

[24] S. Wurster, S. Bigl, M.J. Cordill, D. Kiener, Accelerated thermo-mechanical fatigue of copper metallizations studied by pulsed laser heating, Microelectron. Eng. 167 (2017) 110–118. doi:10.1016/j.mee.2016.08.004.

[25] W. Heinz, W. Robl, G. Dehm, Influence of initial microstructure on thermomechanical fatigue behavior of Cu films on substrates, Microelectron. Eng. 137 (2015) 5–10. doi:10.1016/j.mee.2014.10.024.

[26] T. Walter, G. Khatibi, M. Nelhiebel, W. Heinz, W. Robl, High cycle fatigue properties of Cu films, Microelectron. Eng. 137 (2015) 64–69. doi:10.1016/j.mee.2014.12.003.

35

[27] J.Y. Zhang, X. Zhang, G. Liu, R.H. Wang, G.J. Zhang, J. Sun, Length scale dependent yield strength and fatigue behavior of nanocrystalline Cu thin films, Mater. Sci. Eng. A. 528 (2011) 7774–7780. doi:10.1016/j.msea.2011.06.083.

[28] A.G. Evans, J.W. Hutchinson, The thermomechanical integrity of thin films and multilayers, Acta Metall. Mater. 43 (1995) 2507–2530. doi:10.1016/0956-7151(94)00444-M.

[29] O. Kraft, R. Schwaiger, P. Wellner, Fatigue in thin films: lifetime and damage formation, Mater. Sci. Eng. A. 319–321 (2001) 919–923. doi:10.1016/S0921-5093(01)00990-X.

[30] C.M. Lee, J.P. Chu, W.Z. Chang, J.W. Lee, J.S.C. Jang, P.K. Liaw, Fatigue property improvements of Ti–6Al–4V by thin film coatings of metallic glass and TiN: a comparison study, Thin Solid Films. 561 (2014) 33–37. doi:10.1016/j.tsf.2013.08.027.

[31] G. Cassar, J.C. Avelar-Batista Wilson, S. Banfield, J. Housden, M. Fenech, A. Matthews, A. Leyland, Evaluating the effects of plasma diffusion processing and duplex diffusion/PVD-coating on the fatigue performance of Ti-6Al-4V alloy, Int. J. Fatigue. 33 (2011) 1313–1323. doi:10.1016/j.ijfatigue.2011.04.004.

[32] M.Y.P. Costa, M.L.R. Venditti, M.O.H. Cioffi, H.J.C. Voorwald, V.A. Guimarães, R. Ruas, Fatigue behavior of PVD coated Ti-6Al-4V alloy, Int. J. Fatigue. 33 (2011) 759–765. doi:10.1016/j.ijfatigue.2010.11.007.

[33] C. Kirchlechner, K.J. Martinschitz, R. Daniel, M. Klaus, C. Genzel, C. Mitterer, J. Keckes, Residual stresses and thermal fatigue in CrN hard coatings characterized by high-temperature synchrotron X-ray diffraction, Thin Solid Films. 518 (2010) 2090–2096. doi:10.1016/j.tsf.2009.08.011.

[34] Y. Bai, Y. Xi, K. Gao, H. Yang, X. Pang, X. Yang, A.A. Volinsky, Brittle coating effects on fatigue cracks behavior in Ti alloys, Int. J. Fatigue. 125 (2019) 432–439. doi:10.1016/j.ijfatigue.2019.04.017.

[35] Y. Bai, T. Guo, J. Wang, J. Gao, K. Gao, X. Pang, Stress-sensitive fatigue crack initiation mechanisms of coated titanium alloy, Acta Mater. 217 (2021) 117179. doi:10.1016/j.actamat.2021.117179.

[36] T. Guo, Y. Chen, R. Cao, X. Pang, J. He, L. Qiao, Cleavage cracking of ductile-metal substrates induced by brittle coating fracture, Acta Mater. 152 (2018) 77–85. doi:10.1016/j.actamat.2018.04.017.

[37] N.P. Sivagnanam Chandra, Y. Otsuka, Y. Mutoh, K. Yamamoto, Effect of coating thickness on fatigue behavior of TiAlN coated Ti-alloys, Int. J. Fatigue. 140 (2020) 105767. doi:10.1016/j.ijfatigue.2020.105767.

[38] N.G.P. Sivagnanam Chandra, Y. Otsuka, Y. Mutoh, K. Yamamoto, Fatigue strength and mechanism of Ti6242S titanium alloy with TiAlN coating deposited under various bias voltages, Int. J. Fatigue. 131 (2020) 105338. doi:10.1016/j.ijfatigue.2019.105338.

[39] D. Kiener, C. Motz, W. Grosinger, D. Weygand, R. Pippan, Cyclic response of copper single crystal micro-beams, Scr. Mater. 63 (2010) 500–503.

doi:10.1016/j.scriptamat.2010.05.014.

[40] A. Wimmer, W. Heinz, T. Detzel, W. Robl, M. Nellessen, C. Kirchlechner, G. Dehm, Cyclic bending experiments on free-standing Cu micron lines observed by electron backscatter diffraction, Acta Mater. 83 (2015) 460–469. doi:10.1016/j.actamat.2014.10.012.

[41] S. Lavenstein, B. Crawford, G.-D. Sim, P.A. Shade, C. Woodward, J.A. El-Awady, High frequency in situ fatigue response of Ni-base superalloy René-N5 microcrystals, Acta Mater. 144 (2018) 154–163. doi:10.1016/j.actamat.2017.10.049.

[42] M. Alfreider, D. Kozic, O. Kolednik, D. Kiener, In-situ elastic-plastic fracture mechanics on the microscale by means of continuous dynamical testing, Mater. Des. 148 (2018) 177–187. doi:10.1016/j.matdes.2018.03.051.

[43] D.R. Lide, CRC Handbook of Chemistry and Physics, 84th ed., CRC Press, 2003.

[44] K. Frisk, A thermodynamic evaluation of the Cr-N, Fe-N, Mo-N and Cr-Mo-N systems, Calphad. 15 (1991) 79–106. doi:10.1016/0364-5916(91)90028-I.

[45] P.K. Liao, K.E. Spear, The B-Cr (Boron-Chromium) system, Bull. Alloy Phase Diagrams. 7 (1986) 232–237. doi:10.1007/BF02868996.

[46] L. Kaufman, H. Nesor, Calculation of quasibinary and quasiternary oxide systems — I, Calphad. 2 (1978) 35–53. doi:10.1016/0364-5916(78)90004-4.

[47] G.M. Pharr, An improved technique for determining hardness and elastic modulus using load and displacement sensing indentation experiments, J. Mater. Res. 7 (1992) 1564–1583. doi:10.1557/JMR.1992.1564.

[48] S. Brinckmann, K. Matoy, C. Kirchlechner, G. Dehm, On the influence of microcantilever pre-crack geometries on the apparent fracture toughness of brittle materials, Acta Mater. 136 (2017) 281–287. doi:10.1016/j.actamat.2017.07.014.

[49] J.M. Wheeler, J. Michler, Elevated temperature, nano-mechanical testing in situ in the scanning electron microscope, Rev. Sci. Instrum. 84 (2013) 045103. doi:10.1063/1.4795829.

[50] I.N. Sneddon, The relation between load and penetration in the axisymmetric boussinesq problem for a punch of arbitrary profile, Int. J. Eng. Sci. 3 (1965) 47–57. doi:10.1016/0020-7225(65)90019-4.

[51] J. Keckes, M. Bartosik, R. Daniel, C. Mitterer, G. Maier, W. Ecker, J. Vila-Comamala, C. David, S. Schoeder, M. Burghammer, X-ray nanodiffraction reveals strain and microstructure evolution in nanocrystalline thin films, Scr. Mater. 67 (2012) 748–751. doi:10.1016/j.scriptamat.2012.07.034.

[52] M. Birkholz, Thin Film Analysis by X-Ray Scattering, Wiley, 2006. doi:10.1002/3527607595.

[53] J. Almer, U. Lienert, R.L. Peng, C. Schlauer, M. Odén, Strain and texture analysis of coatings using high-energy x-rays, J. Appl. Phys. 94 (2003) 697–702.

doi:10.1063/1.1582351.

[54]   G. Benecke, W. Wagermaier, C. Li, M. Schwartzkopf, G. Flucke, R. Hoerth, I. Zizak, M. Burghammer, E. Metwalli, P. Müller-Buschbaum, M. Trebbin, S. Förster, O. Paris, S. V. Roth, P. Fratzl, A customizable software for fast reduction and analysis of large X-ray scattering data sets: Applications of the new DPDAK package to small-angle X-ray scattering and grazing-incidence small-angle X-ray scattering, J. Appl. Crystallogr. 47 (2014) 1797–1803. doi:10.1107/S1600576714019773.

[55]   L. Zauner, A Matlab Toolbox for Synchrotron Stress Analysis, 2022. doi:10.5281/ZENODO.6248169.

[56]   ICDD, Powder Diffraction File - cubic Cr - 00-006-0694, Powder Diffr. File - Cubic Cr - 00-006-0694. (1970).

[57]   ICDD, Powder Diffraction File - cubic CrN - 01-077-0047, Powder Diffr. File - Cubic CrN - 01-077-0047. (2015).

[58]   ICDD, Powder Diffraction File - hexagonal CrB2 - 04-004-1734, Powder Diffr. File - Hexag. CrB2 - 04-004-1734. (2011).

[59]   ICDD, Powder Diffraction File - rhombohedral Cr2O3 - 00-006-0504, Powder Diffr. File - Rhombohedral Cr2O3 - 00-006-0504. (1970).

[60]   ICDD, Powder Diffraction File - cubic Si - 00-027-1402, Powder Diffr. File - Cubic Si - 00-027-1402. (2017).

[61]   A. Anders, A structure zone diagram including plasma-based deposition and ion etching, Thin Solid Films. 518 (2010) 4087–4090. doi:10.1016/j.tsf.2009.10.145.

[62]   S. Zare Chavoshi, P.S. Branicio, Q. An, Transition between Hall-Petch and inverse Hall-Petch behavior in nanocrystalline silicon carbide, Phys. Rev. Mater. 5 (2021) 073606. doi:10.1103/PhysRevMaterials.5.073606.

[63]   M. Bartosik, R. Hahn, Z.L. Zhang, I. Ivanov, M. Arndt, P. Polcik, P.H. Mayrhofer, Fracture toughness of Ti-Si-N thin films, Int. J. Refract. Met. Hard Mater. 72 (2018) 78–82. doi:10.1016/j.ijrmhm.2017.12.015.

[64]   F. Konstantiniuk, M. Tkadletz, C. Kainz, C. Czettl, N. Schalk, Mechanical properties of single and polycrystalline α-Al2O3 coatings grown by chemical vapor deposition, Surf. Coatings Technol. 410 (2021) 126959. doi:10.1016/j.surfcoat.2021.126959.

[65]   R. Wadsack, R. Pippan, B. Schedler, Chromium - A material for fusion technology, Fusion Eng. Des. 58–59 (2001) 743–748. doi:10.1016/S0920-3796(01)00554-3.

[66]   E. Bitzek, J.R. Kermode, P. Gumbsch, Atomistic aspects of fracture, Int. J. Fract. 191 (2015) 13–30. doi:10.1007/s10704-015-9988-2.

[67]   H. Kindlund, D.G. Sangiovanni, I. Petrov, J.E. Greene, L. Hultman, A review of the intrinsic ductility and toughness of hard transition-metal nitride alloy thin films, Thin Solid Films. 688 (2019) 137479. doi:10.1016/j.tsf.2019.137479.

[68] K. Balasubramanian, S. V. Khare, D. Gall, Valence electron concentration as an indicator for mechanical properties in rocksalt structure nitrides, carbides and carbonitrides, Acta Mater. 152 (2018) 175–185. doi:10.1016/j.actamat.2018.04.033.

[69] C. Fuger, R. Hahn, L. Zauner, T. Wojcik, M. Weiss, A. Limbeck, O. Hunold, P. Polcik, H. Riedl, Anisotropic super-hardness of hexagonal WB2±z thin films, Http://Mc.Manuscriptcentral.Com/Tmrl. 10 (2022) 70–77. doi:10.1080/21663831.2021.2021308.

[70] V.L. Deringer, A.L. Tchougréeff, R. Dronskowski, Crystal orbital Hamilton population (COHP) analysis as projected from plane-wave basis sets, J. Phys. Chem. A. 115 (2011) 5461–5466. doi:10.1021/jp202489s.

[71] R. Fritz, V. Maier-Kiener, D. Lutz, D. Kiener, Interplay between sample size and grain size: Single crystalline vs. ultrafine-grained chromium micropillars, Mater. Sci. Eng. A. 674 (2016) 626–633. doi:10.1016/j.msea.2016.08.015.

[72] F.F. Csikor, C. Motz, D. Weygand, M. Zaiser, S. Zapperi, Dislocation avalanches, strain bursts, and the problem of plastic forming at the micrometer scale, Science (80-.). 318 (2007) 251–254. doi:10.1126/science.1143719.

[73] S.-Y. Liu, I.-W. Chen, Fatigue of Yttria-Stabilized Zirconia: II, Crack Propagation, Fatigue Striations, and Short-Crack Behavior, J. Am. Ceram. Soc. 74 (1991) 1206–1216. doi:10.1111/j.1151-2916.1991.tb04089.x.

[74] X.M. Luo, X.F. Zhu, G.P. Zhang, Nanotwin-assisted grain growth in nanocrystalline gold films under cyclic loading, Nat. Commun. 5 (2014) 1–8. doi:10.1038/ncomms4021.